Plasma versus thermal annealing for the Au-catalyst growth of ZnO nanocones and nanowires on Al-doped ZnO buffer layers

You may also be interested in:

Materials Research Express

Plasma versus thermal annealing for the Au-catalyst growth of ZnO nanocones and nanowires on Al-doped ZnO buffer layers

Frank Güell[1], Paulina R Martínez-Alanis[1], Sergio Roso[1], Carlos I Salas-Pérez[2], Mario F García-Sánchez[3], Guillermo Santana[2] and B Marel Monroy[2]

1   Departament d'Enginyeries: Electrònica, Universitat de Barcelona, C/Martí i Franquès 1, E-08028 Barcelona, Catalunya, Spain
2   Instituto de Investigaciones en Materiales, Universidad Nacional Autónoma de México, Ciudad Universitaria, 04510 D.F., Mexico
3   Unidad Profesional Interdisciplinaria en Ingeniería y Tecnologías Avanzadas, Instituto Politécnico Nacional, Av. I.P.N. 2580, Gustavo A. Madero, 07340 D.F., Mexico

E-mail: frank@el.ub.edu

Abstract

We successfully synthesized ZnO nanocones and nanowires over polycrystalline Al-doped ZnO (AZO) buffer layers on fused silica substrates by a vapor-transport process using Au-catalyst thin films. Different Au film thicknesses were thermal or plasma annealed in order to analyze their influence on the ZnO nanostructure growth morphology. Striking differences have been observed. Thermal annealing generates a distribution of Au nanoclusters and plasma annealing induces a fragmentation of the Au thin films. While ZnO nanowires are found in the thermal-annealed samples, ZnO nanocones and nanowires have been obtained on the plasma-annealed samples. Enhancement of the preferred c-axis (0001) growth orientation was demonstrated by x-ray diffraction when the ZnO nanocones and nanowires have been grown over the AZO buffer layer. The transmittance spectra of the ZnO nanocones and nanowires show a gradual increase from 375 to 900 nm, and photoluminescence characterization pointed out high concentration of defects leading to observation of a broad emission band in the visible range from 420 to 800 nm. The maximum emission intensity peak position of the broad visible band is related to the thickness of the Au-catalyst for the thermal-annealed samples and to the plasma power for the plasma-annealed samples. Finally, we proposed a model for the plasma versus thermal annealing of the Au-catalyst for the growth of the ZnO nanocones and nanowires. These results are promising for renewable energy applications, in particular for its potential application in solar cells.

1. Introduction

One-dimensional nanostructures such as nanowires (NWs) have attracted a lot of attention compared to bulk and thin film materials, due to their high surface-to-volume ratio, which increases their response to light. ZnO NWs show remarkable optical properties such as an efficient third harmonic ultraviolet (UV) generation [1]; and have multitude of applications including UV lasers [2], light emitting diodes [3] and solar cells [4]. ZnO thin films have been applied as a transparent conductive oxide and anti-reflective coating layer (refractive index of 2.0) in photovoltaic devices. Al-doped ZnO (AZO) buffer layers are attractive owing to their good conductivity, high transparency and relatively low cost. AZO buffer layers can be prepared by a variety of thin film deposition techniques such as radio frequency magnetron sputtering [5], pulsed-laser deposition [6], and spray pyrolysis [7]. Spray pyrolysis is the less costly one and well adapted for mass fabrication. ZnO NWs grown over AZO buffer layers exhibited better dye-sensitized solar cells performances than those grown on fluorine doped tin oxide thin films [8].

Several growth methods have been reported in the literature for the production of ZnO NWs such as hydrothermal [9], electrochemical [10] and vapor-transport [11]. Vapor-transport processes normally require the use of Au as catalyst in order to induce assisted growth by the vapor–liquid–solid (VLS) mechanism [12–14].

Table 1. Experimental details of the Au-catalyst films deposited on the AZO buffer layers over fused silica substrates, and of the VLS assisted growth of the ZnO NCs and NWs and the NBE.

Au/ AZO/ SiO$_2$ Sample number	Au-catalyst				ZnO NC and NWs		NBE	
	Film thickness (nm)	Annealing	Nanocluster diameter (nm)	Nanocluster density (μm^{-2})	Diameter (nm)	Density (μm^{-2})	Peak (nm)/(eV)	FWHM (meV)
1	4	Thermal	40	190 ± 5	100	22 ± 2	385/3.22	220
2	7	"	70	60 ± 4	110	21 ± 1	384/3.23	150
3	10	"	80	30 ± 3	130	17 ± 1	383/3.24	120
4	15	"	—	—	140	10 ± 1	382/3.25	120
5	7	NH$_3$ (50 W)	—	—	110	20 ± 2	383/3.24	150
6	15	"	—	—	130	14 ± 2	384/3.23	130
7	7	NH$_3$ (100 W)	—	—	—	—	—	—
8	15	"	—	—	100	33 ± 4	385/3.22	150
9	7	NH$_3$ + H$_2$ (100 W)	—	—	110	11 ± 2	386/3.21	150

The influence of the thermal annealing for the Au-catalyst growth of ZnO NWs has been methodically explored [15]. Size control over the ZnO NW diameters has been already achieved by varying the thickness of the Au-catalyst films [16]. Previously works demonstrate that the application of cold plasma on Au films under certain conditions generates small Au nanoclusters [17, 18]. This was obtained by two different ways: increasing the plasma time exposure or changing the plasma chemistry. Since today, studies of plasma treatments on the Au-catalyst films previous the growth of ZnO NWs by the VLS process remains to be explored.

In this work we compared the influence of the thermal versus plasma annealing for the Au-catalyst growth of ZnO nanostructures on AZO buffer layers over fused silica substrates. The ZnO nanocones (NCs) and NWs obtained have been characterized by field-emission scanning electron microscopy (FESEM), x-ray diffraction (XRD), UV–visible transmittance and photoluminescence (PL) spectroscopy. We proposed a model for the growth of the ZnO NCs and NWs using the Au-catalyst thin films thermal or plasma annealed.

2. Experimental details

2.1. AZO buffer layer deposition
AZO buffer layers with thicknesses at around 250 nm were deposited on fused silica substrates by spray pyrolysis at 475 °C during 10 min. A solution of zinc acetylacetonate (Zn[O$_2$C$_5$H$_7$]$_2$) and aluminum acetylacetonate (Al[O$_2$C$_5$H$_7$]$_3$) in a mixture of methanol and water at 0.1 M was used in the pyrolytic process. The amount of aluminum in solution was 4.45 atomic%. The carrier and director gas flow rates were fixed at 1.0 l min^{-1} and 3.5 l min^{-1}, respectively.
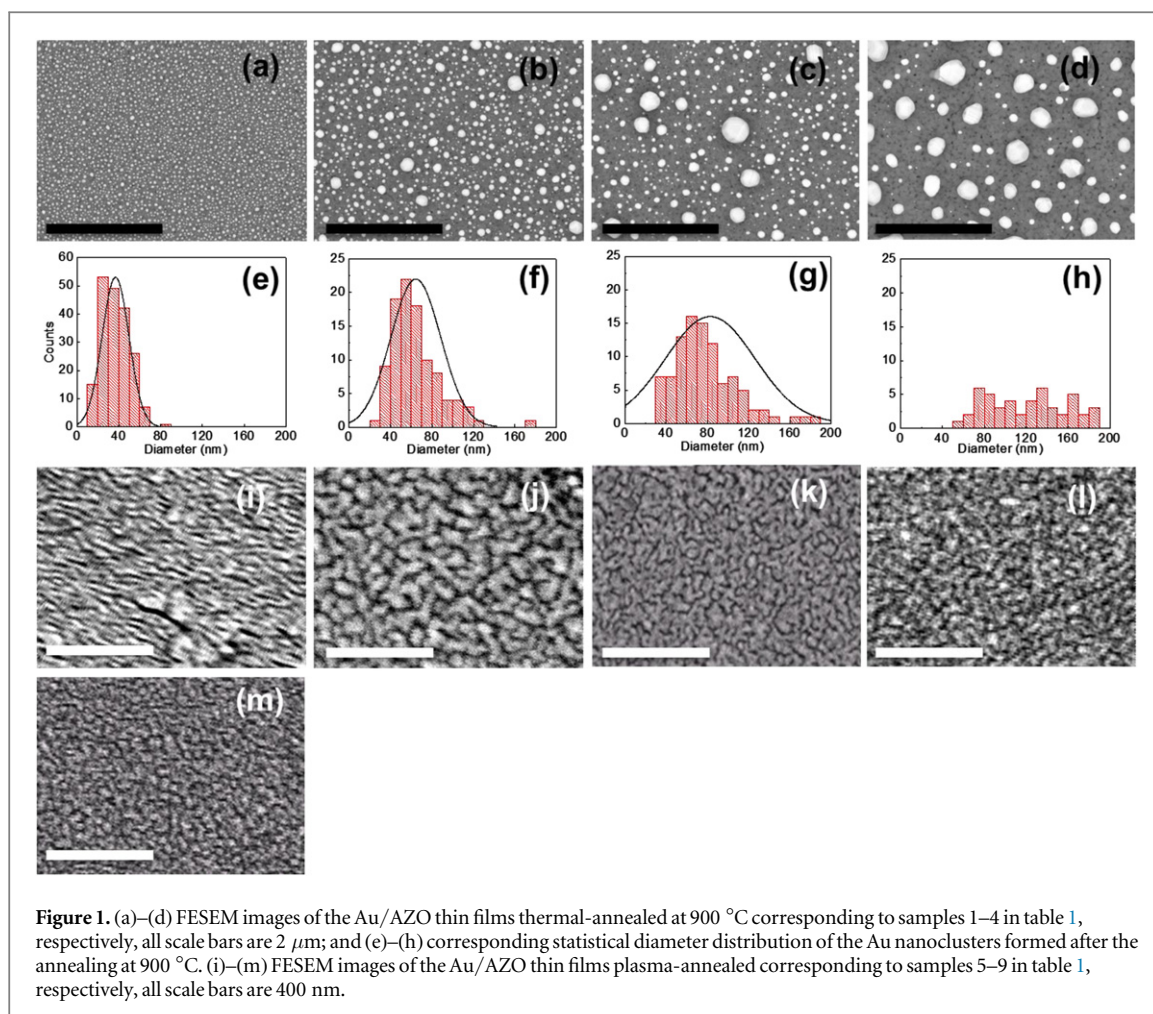
2.2. Au-catalyst deposition
Au thin films with various nominal thicknesses of 4, 7, 10 and 15 nm (table 1) were deposited over the AZO buffer layers by physical vapor deposition, with a pressure of around 1 μTorr and an Au target of 99.99% purity. The Au film thickness was controlled with a deposition controller Telemark model 860 with and evaporation rate of 0.1 Å s^{-1}. The substrate temperature was fixed at 300 °C.

2.3. Au-catalyst annealing process
The Au thin films were annealed using two different procedures: (i) at high temperature (900 °C) in a tubular furnace under Ar atmosphere for 30 min, and (ii) at lower temperature (200 °C) in NH$_3$ or NH$_3$ + H$_2$ plasma for 5 min with a pressure of 250 mTorr and a gas flow of 25 sccm. The radio frequency powers used were 50 and 100 W (table 1).

2.4. Synthesis of ZnO NCs and NWs
ZnO NCs and NWs were grown on the pretreated surfaces of the Au/AZO thin films over fused silica substrates. ZnO powder was mixed with graphite powder of 1:1 mole ratio and the synthesis was carried out in a horizontal quartz tube placed in a chemical vapor deposition (CVD) furnace. Argon was used as an inert gas and the furnace was heated from room temperature to 900 °C, remained at 900 °C for 30 min, and then naturally cooled down to room temperature. The powder mixture and the pretreated substrate were placed in the center of the furnace,

Figure 1. (a)–(d) FESEM images of the Au/AZO thin films thermal-annealed at 900 °C corresponding to samples 1–4 in table 1, respectively, all scale bars are 2 μm; and (e)–(h) corresponding statistical diameter distribution of the Au nanoclusters formed after the annealing at 900 °C. (i)–(m) FESEM images of the Au/AZO thin films plasma-annealed corresponding to samples 5–9 in table 1, respectively, all scale bars are 400 nm.

where the heating temperature was the highest. The argon gas flow was 400 sccm and the pressure inside the tube was maintained at 760 Torr during all the process.

2.5. Structural and optical characterization

The surface morphology of the Au thin films annealed and the ZnO nanostructures obtained have been characterized using FESEM with a Jeol JSM-7600F and a Hitachi H-4100FE, respectively. Their crystal structure was analyzed by XRD with a copper anticathode (Cu Kα, 1.54 Å) model Bruker AXS D8 Advance. The UV–visible transmittance spectra at room temperature were performed using a Jasco V-630 spectrometer in the wavelength range 320–900 nm, and the room-temperature PL measurements were made with a chopped Kimmon IK Series He–Cd laser (325 nm and 40 mW). Fluorescence was dispersed through an Oriel Corner Stone 1/8 74000 monochromator, detected with a Hamamatsu R928 photomultiplier, and amplified through a Stanford Research Systems SR830 DSP lock-in amplifier. A 360 nm filter was used for filtering the stray light. It is worth pointing out that all the emission spectra were corrected using the optical transfer function of the PL setup.

3. Results and discussion

Table 1 summarizes the samples studied in this work: samples 1–4 were thermal-annealed at 900 °C with different Au film thicknesses of 4, 7, 10 and 15 nm, respectively; and samples 5–9 were plasma-annealed with NH_3 or NH_3+H_2 at powers of 50 or 100 W with Au film thicknesses of 7 or 15 nm. Figures 1(a)–(d) show the FESEM images of the Au/AZO surface morphology after the thermal annealing at 900 °C corresponding to samples 1–4, respectively. For all the samples the thermal annealing generates a distribution of Au nanoclusters all over the AZO surface. Figure 1(a) illustrates that the thinner Au film generates the smaller and most uniformly sized Au nanoclusters, and figure 1(d) shows that the thicker Au film leads to bigger Au nanoclusters. Figures 1(e)–(h) present the statistical diameter distribution of the resulting Au nanoclusters for samples 1–4, respectively. The Au nanoclusters have average diameters of 40, 70 and 80 nm, and densities at around 190 ± 5,
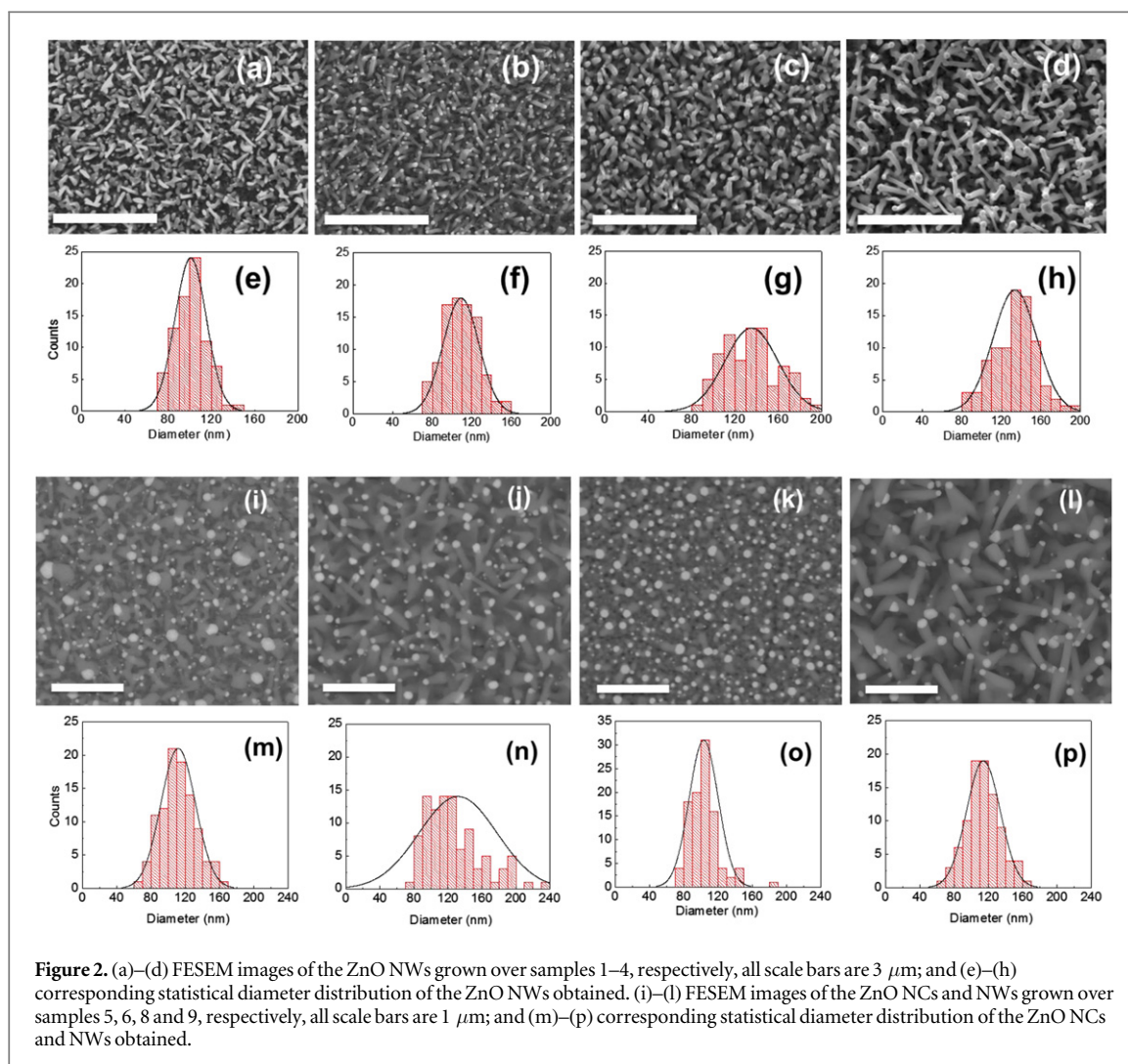
Figure 2. (a)–(d) FESEM images of the ZnO NWs grown over samples 1–4, respectively, all scale bars are 3 μm; and (e)–(h) corresponding statistical diameter distribution of the ZnO NWs obtained. (i)–(l) FESEM images of the ZnO NCs and NWs grown over samples 5, 6, 8 and 9, respectively, all scale bars are 1 μm; and (m)–(p) corresponding statistical diameter distribution of the ZnO NCs and NWs obtained.

60 $\pm$ 4 and 30 $\pm$ 3 nanoclusters μm^{-2} for the 4, 7 and 10 nm thick Au films, respectively (table 1). The Au nanoclusters sizes plotted in figure 1(h) cannot be described by a mean diameter due to the high dispersion in sizes for the 15 nm thick Au film. The coalescence of the Au nanoclusters produced by the thermal induced dewetting is usually accounted for by considering either Ostwald ripening or droplet coalescence mechanisms [15]. Since droplet coalescence favors high particle densities with small sizes, this is the predominant mechanism in samples 1–3. For sample 4, Ostwald ripening could also be present, which explains the high size dispersion observed. Figures 1(i)–(m) show the FESEM images illustrating the Au/AZO surface morphology after the plasma annealing corresponding to samples 5–9, respectively. For all the samples the plasma annealing induces a fragmentation of the Au thin film, and no formation of Au nanoclusters was observed on the AZO surface. At the same plasma power of 50 W, less fragmentation was observed if the Au film is thicker as shown in figure 1(j). However, this was not observed increasing the plasma power up to 100 W. Samples 7–9 with Au film thicknesses of 7 or 15 nm exhibit similar fragmentation on the surface (figures 1(k)–(m)).

The procedures continued placing the pretreated surfaces of the Au/AZO thin films in the CVD furnace together with the ZnO/carbon powder mixture and the synthesis was carried out at 900 °C. Successfully growth of ZnO NWs takes place over samples 1–4 (figures 2(a)–(d)). The FESEM images revealed formation of a dense forest of ZnO NWs lacking vertical alignment due to the polycrystalline nature of the AZO surface. As expected in the context of the VLS mechanism, the size of the Au nanoclusters influences on the growth of the ZnO NWs. The average length of the ZnO NWs in all the samples is around 0.5 μm, and their corresponding statistical diameter distributions are plotted in figures 2(e)–(h). The wire diameters range from 70 to 200 nm, and the obtained average diameters are around 100, 110, 130 and 140 nm for samples 1 to 4, respectively (table 1). As expected ZnO NWs with bigger diameters were obtained when increasing the thickness of the Au-catalyst films. Moreover, as can be seen in figures 2(a)–(d), the density of the ZnO NWs decreases as the thickness of the Au film increases. We found densities of 22 $\pm$ 2, 21 $\pm$ 1, 17 $\pm$ 1 and 10 $\pm$ 1 wires μm^{-2} for samples 1–4, respectively (table 1). Changing the thickness of the Au-catalyst films we are able to control the diameters and density of the
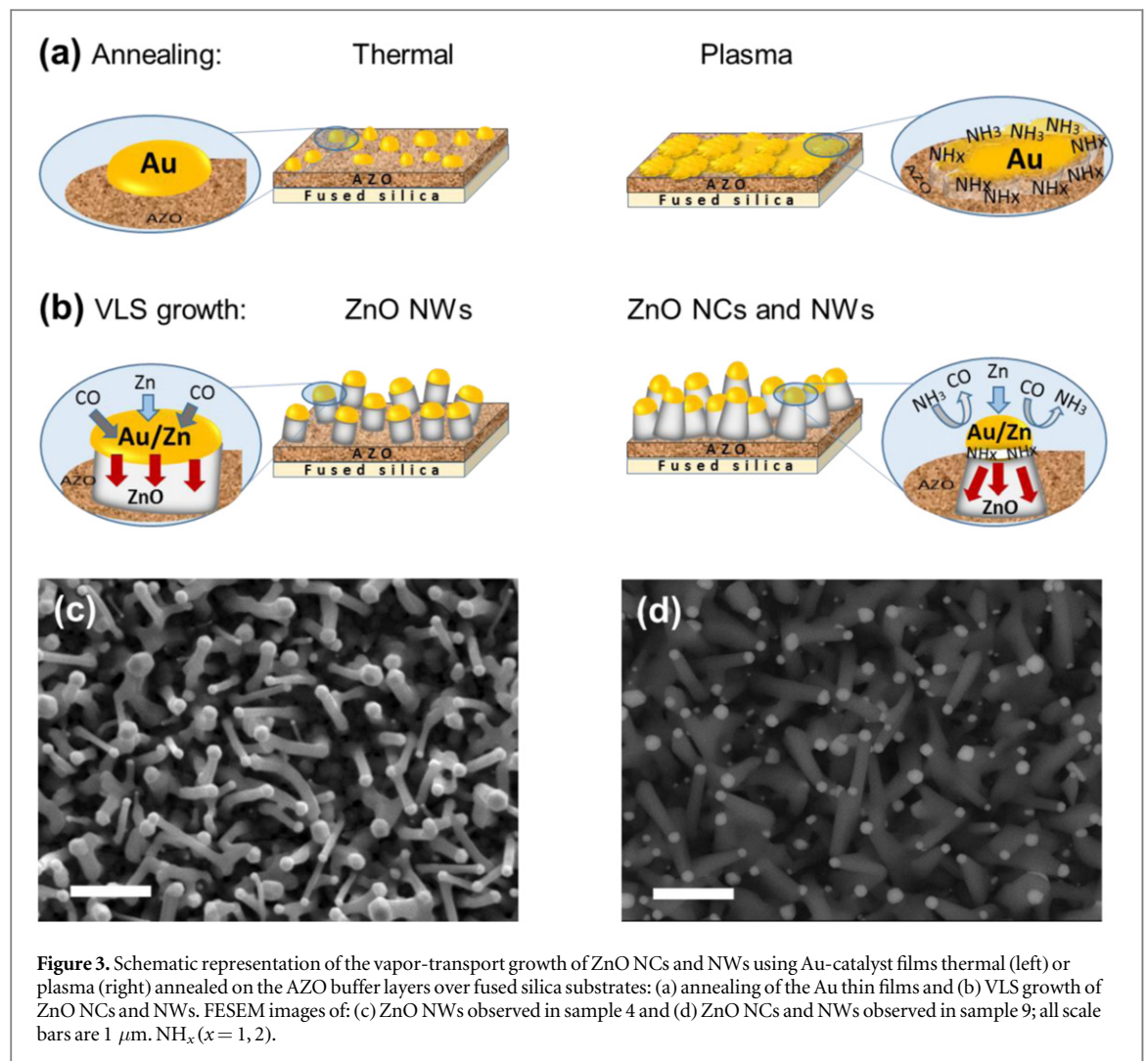
Figure 3. Schematic representation of the vapor-transport growth of ZnO NCs and NWs using Au-catalyst films thermal (left) or plasma (right) annealed on the AZO buffer layers over fused silica substrates: (a) annealing of the Au thin films and (b) VLS growth of ZnO NCs and NWs. FESEM images of: (c) ZnO NWs observed in sample 4 and (d) ZnO NCs and NWs observed in sample 9; all scale bars are 1 μm. NH$_x$ ($x = 1, 2$).

ZnO NWs obtained. The smaller Au nanoclusters previously formed during the annealing process in sample 1 (figure 1(a)), favors the growth of the high-density and thinner ZnO NWs in the VLS reaction (figure 2(a)). Interestingly, for the plasma-annealed samples not only ZnO NWs have been obtained also ZnO NCs have been grown. Figures 2(i)–(l) show the FESEM images of the ZnO NCs and NWs grown over the plasma-annealed samples 5, 6, 8 and 9, respectively, which revealed formation of a dense forest of ZnO NCs and NWs lacking vertical alignment due to the polycrystalline nature of the AZO surface. Surprisingly, no ZnO nanostructure growth was observed in sample 7, in which the VLS synthesis was carried out at the same conditions of samples 5, 6, 8 and 9, and the difference was only in the pretreatment with NH$_3$ plasma at 100 W (table 1). The fragmentation of the Au thin film influences the growth details of the ZnO NCs and NWs obtained. The average length in all the samples is around 0.5 μm, and their corresponding statistical diameter distributions are plotted in figures 2(m)–(p). The cone and wire diameters range from 70 to 240 nm; their corresponding average diameters are around 110, 130, 100 and 110 nm; and their densities are around 20 ± 2, 14 ± 2, 33 ± 4 and 11 ± 2 nanostructures μm^{-2} for samples 5, 6, 8 and 9, respectively (table 1). At plasma powers of 50 W, the density depends on the thickness of the Au film, increases as the Au film thickness decreases, as was previously observed in the thermal-annealed samples. At plasma powers of 100 W: (i) no ZnO nanostructure growth was observed for sample 7 with an Au film thickness of 7 nm; (ii) high-density ZnO NCs and NWs were obtained for sample 8 with an Au film thickness of 15 nm, see figure 2(k); and (iii) when introducing H$_2$ to the NH$_3$ plasma ZnO NCs and NWs were obtained for sample 9 with a film thickness of 7 nm (figure 2(l)).

Taking into account the results obtained, we proposed a model for the ZnO NCs and NWs grown on the thermal versus plasma annealed samples (figure 3). For the thermal-annealed samples, the diameters of the obtained ZnO NWs are larger than the corresponding Au nanocluster sizes (table 1). This is due to the coalescence effect from the formation of supersaturated Au–Zn alloy liquid droplets in the VLS growth process (figure 3 left). The VLS process involves the reduction of ZnO powder by graphite to form Zn and CO vapor at a high temperature:

$$ZnO_{(s)} + C_{(s)} \rightarrow Zn_{(v)} + CO_{(v)}, \tag{1}$$

$$ZnO_{(s)} + CO_{(v)} \rightarrow Zn_{(v)} + CO_{2(v)}. \tag{2}$$
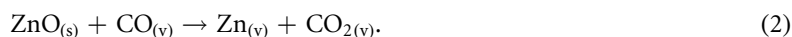
The Zn vapor is transported and reacts with the Au-catalyst on the AZO buffer layer to form Au/Zn alloy liquid droplets. As the droplets become supersaturated of Zn, solid ZnO NWs are formed by the reaction between Zn and CO in vapor (figure 3(b) left):

$$CO_{(v)} + Zn_{(v)} \rightarrow C_{(s)} + ZnO_{(s)}. \tag{3}$$

Also, other chemical reactions took place:

$$C_{(s)} + CO_{2(v)} \rightarrow 2CO_{2(v)}, \tag{4}$$

$$CO_{(v)} \rightarrow O_{2(v)} + C_{(s)}, \tag{5}$$

$$ZnO_{(s)} + CO_{(v)} \rightarrow Zn_{(v)} + CO_{2(v)}. \tag{6}$$
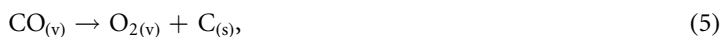
The presence of a small amount of CO is not expected to significantly change the Au/Zn phase diagram, at the same time acts as the oxygen source during the ZnO NW growth. In fact, control experiments with samples without the Au-catalyst essentially produced no ZnO NWs over the AZO buffer layers. Note that the ZnO NWs obtained have diameters thinner compared to their Au-catalyst tips as expected in the VLS growth process (figure 3(c)). For the plasma-annealed samples (figure 3 right), the NH_3 plasma generates a fragmentation of the Au thin film, and introduces NH_3, NH_2 and NH on the Au surface by the following reactions:

$$2NH_{3(v)} \rightarrow 2NH_{2(v)} + H_{2(v)}, \tag{7}$$

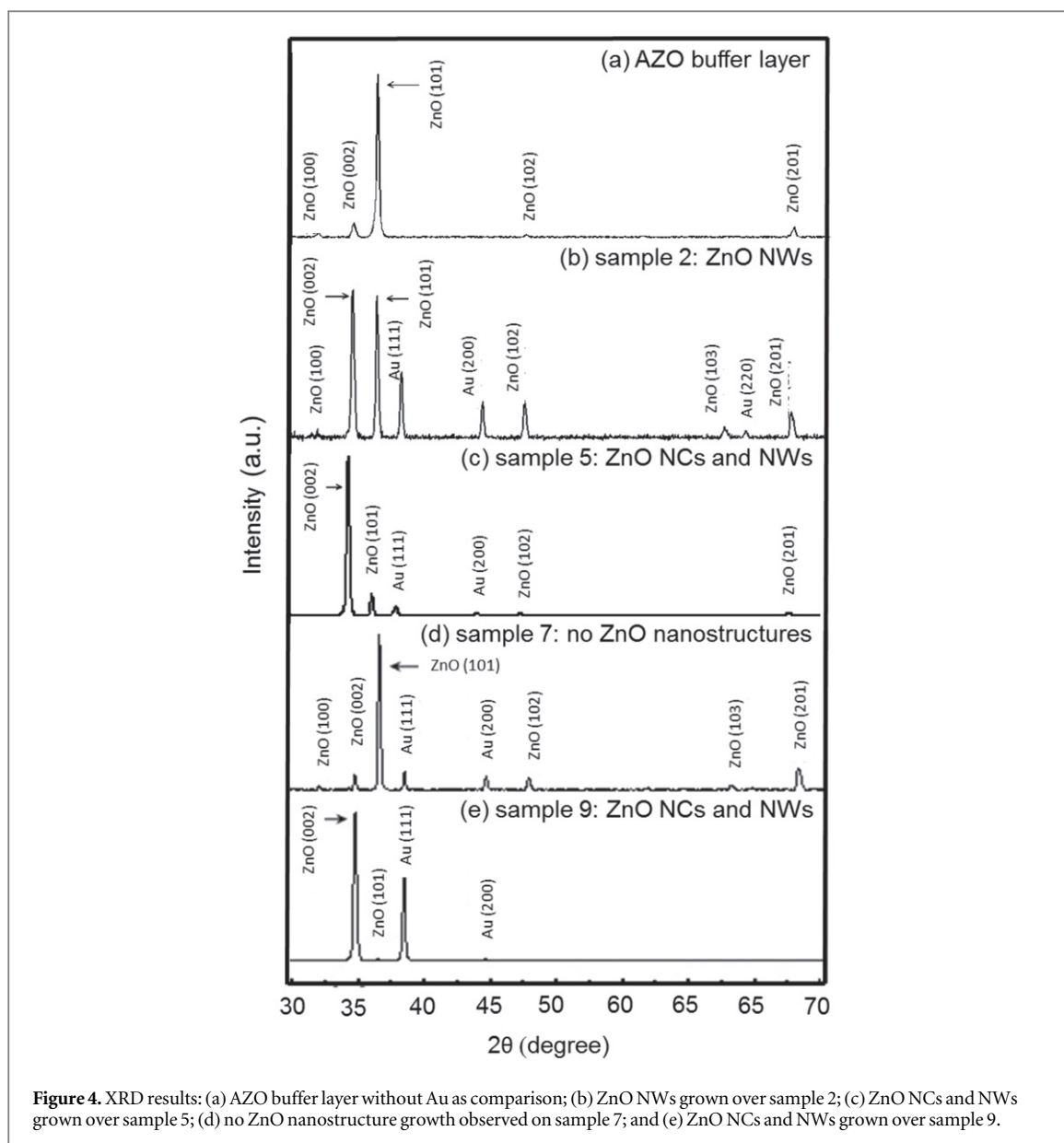$$2NH_{3(v)} \rightarrow 2NH_{(v)} + 2H_{2(v)}. \tag{8}$$

Preferentially the NH_2 and NH will be bonded to the low coordinated Au atoms in the fragmented areas, and the NH_3 will be bonded to the rest of the Au surface [19, 20] (figure 3(a) right). When the Au-catalyst plasma-annealed react with the ZnO and graphite in the CVD furnace, reactions (1)–(6) take place and additionally part of the NH_3 can react with oxygen by the following reaction [21]:

$$2NH_{3(v)} + 2O_{2(v)} \rightarrow 2NO_{2(v)} + 3H_{2(v)}. \tag{9}$$
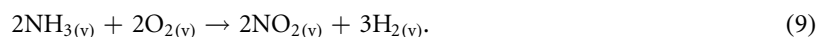
The NH_3, NH_2, NH and NO_2 will compete with the CO to be adsorbed by the Au-catalyst. This fact makes that the oxygen availability for the ZnO nanostructure growth will be affected. Brewster and co-workers have found that the amount of oxygen available is crucial in whether the ZnO NW growth process is Au-assisted or not [22]. Density functional theory studies show that the energy adsorption of the CO, NH_3 and NO_2 over Au nanoclusters is similar, but for NH_2 and NH is around 10 times higher [23, 24]. Then, during the VLS growth process the NH_2 and NH bonded to the low coordinated Au atoms will be at the Au/Zn–AZO interface, and gradually they will diminish the contact area where the Au/Zn alloy droplet is supersaturated with Zn, and the solid ZnO NCs and NWs are formed (figure 3(b) right). This is the reason of the conical shape in the ZnO NCs obtained and why the ZnO NWs have diameters larger compared to their Au-catalyst tips (figure 3(d)). When the Au-catalyst is over damage by the plasma annealing, all the fragmented areas will be filled with NH_2 and NH, and do not allow the CO interaction with the Au-catalyst and the growth of ZnO nanostructures, as it was observed in sample 7. On the other hand, this effect is compensated when H_2 is added to the NH_3 plasma. The presence of H_2 in the plasma annealing not favored reactions (7) and (8), and allows the growth of ZnO NCs and NWs, as it was observed in sample 9 (figure 2(l)).

The crystal structure of the ZnO NCs and NWs grown over the AZO buffer layers was analyzed by XRD. Figure 4 displays typical XRD data of the ZnO NCs and NWs in comparison to the AZO buffer layer. For the AZO buffer layer, the dominant XRD reflection at around 36.67° is associated with the ZnO (101) reflection, which is ascribed to the wurzite hexagonal shaped ZnO (figure 4(a)). The polycrystalline AZO buffer layer yields a larger proportion of inclined grains, which gives rise to a weaker ZnO (002) peak. For the thermal-annealed samples, an enhancement of the XRD reflection at around 34.84° associated with the ZnO (002) reflection appears confirming the preferential growth direction for the ZnO NWs along the *c*-axis (0001) (figure 4(b)). The ZnO (101) reflection from the AZO buffer layer is present with similar intensity to the ZnO (002) reflection and other reflections from the Au at (111), (200) and (220) appeared from the Au-catalyst tips of the ZnO NWs. The presence of additional ZnO peaks at (100), (102), (103) and (201) reflections reveal that the ZnO NWs are not vertically oriented, as can be seen in figures 2(a)–(d). For the plasma-annealed samples, the ZnO (101) reflection notably diminishes respect to the ZnO (002) reflection confirming the preferential growth direction for the ZnO NCs and NWs along the *c*-axis (0001) (figures 4(c) and (e)). Also, it can be seen the Au reflections at (111) and (200) from the Au-catalyst tips of the ZnO NCs and NWs and the additional ZnO reflections at (100), (102) and (201). On sample 7, were no ZnO nanostructure growth was observed, the dominant reflection is the ZnO (101) from the AZO buffer layer; and also Au reflections at (111) and (200) can be seen from the Au-catalyst plasma-annealed (figure 4(d)). The Au reflections in the plasma-annealed samples can be seen with lower intensity respect to the thermal-annealed samples, which could be associated to the coordination of the NH_2 and NH to

Figure 4. XRD results: (a) AZO buffer layer without Au as comparison; (b) ZnO NWs grown over sample 2; (c) ZnO NCs and NWs grown over sample 5; (d) no ZnO nanostructure growth observed on sample 7; and (e) ZnO NCs and NWs grown over sample 9.

the Au-catalyst. When H_2 is added to the NH_3 plasma, an enhancement of the Au reflection at (111) is observed which allows the growth of ZnO NCs and NWs in sample 9 (figure 4(e)). This result corroborates the importance of the crystallinity of the Au-catalyst for the growth of the ZnO NCs and NWs. Note that the initial Au-catalyst film thickness is 7 nm for samples 2, 5, 7 and 9 (table 1), which correspond to the XRD results presented in figure 4.

Optical techniques were employed with the aim of assessing the crystal quality of the obtained ZnO NCs and NWs. The transmittance measurements like a measurement of the optical transparency of the thermal or plasma-annealed samples are show in figure 5. Figures 5(a) and (c) show the transmittance spectra for the thermal-annealed samples 1–4 and the plasma-annealed samples 5, 6, 8 and 9, respectively, previous the VLS growth of the ZnO NCs and NWs. The transmittance spectrum of the AZO buffer layer without Au over fused silica substrates is plotted in figure 5(a) for comparison. The AZO buffer layers exhibit a transmittance below 90% along all the visible range and near infrared (400–900 nm) and a sharp decrease of transmittance occurs at around 375 nm (3.30 eV). Its fluctuation in the spectral shape should be ascribed to interference phenomenon between the top and the bottom surface of the AZO buffer layer. The absorption-edge shifts observed at around 375 nm for the thermal-annealed samples 1–4 are because absorption due to d electron transitions dominates the optical properties of the Au thin layers below 400 nm [25]. As expected, the transmittance spectra decrease as the thickness of the Au layer increases for all the samples. Also, the transmittance spectra decrease in the 500–750 nm visible range due to surface plasmon resonances (SPR) from the Au-catalyst. This phenomenon has been observed both in isolated Au nanoclusters of diameters less than 100 nm and in non-uniform Au layers
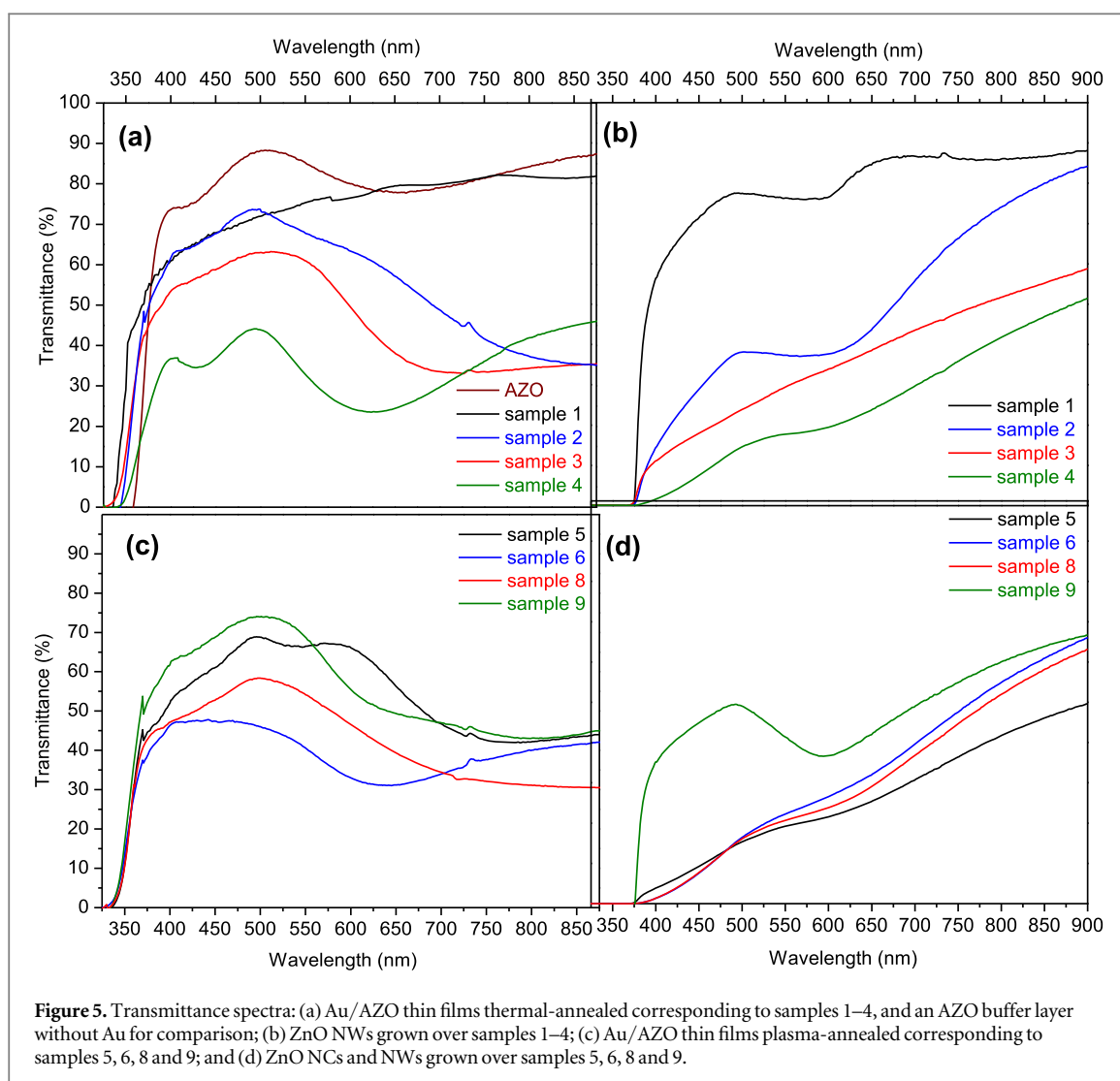
Figure 5. Transmittance spectra: (a) Au/AZO thin films thermal-annealed corresponding to samples 1–4, and an AZO buffer layer without Au for comparison; (b) ZnO NWs grown over samples 1–4; (c) Au/AZO thin films plasma-annealed corresponding to samples 5, 6, 8 and 9; and (d) ZnO NCs and NWs grown over samples 5, 6, 8 and 9.

formed by an irregular metallic network as in our case [26], as can be seen in figures 1(a)–(d) and (i)–(m), respectively. The spectral position of the SPR depends on three main parameters: (i) the diameter of the Au nanoclusters, (ii) the particle density, and (iii) the surface roughness (associated with the Au nanoclusters height), all of which redshift the SPR spectral position as they increase. Our transmittance results can be explained in terms of SPR redshifts induced by increasing the Au nanoclusters size, or SPR blue shifts associated with decreasing the surface roughness of the Au-catalyst. Figures 5(b) and (d) shows the transmittance spectra of the ZnO NCs and NWs grown on the Au/AZO thin films thermal or plasma annealed, respectively. In general a decrease of shape in the transmittance spectrum is observed compared with the results obtained for the Au/AZO thin films in figures 5(a) and (c). This decrease is attributed to the scattering of light on the surface owing to the increase in surface roughness and thickness by the ZnO NCs and NWs. Also, since the Au-catalyst is at the tips of the ZnO NCs and NWs, absorption due to SPR effects is also observed.

Figures 6(a) and (b) shows the PL emission spectra of the ZnO NCs and NWs grown on samples 1–4 and 5, 6, 8 and 9, respectively. By pumping at 325 nm, two main bands are observed: one characteristic sharp emission in the UV and a broad emission in the visible region. While the UV emission peak corresponds to the near band-edge (NBE) transition, which is associated to exciton recombination processes [16], the visible emission band is commonly referred to as a deep-level (DL), trap-state or impurity-related radiative recombination process [12]. The NBE/DL ratio is an important factor used for comparing the crystal-quality between samples [27]. The NBE/DL ratio is maximum for the thermal-annealed sample 2 and the plasma-annealed sample 6. Then, the ZnO NWs grown on the thermal-annealed sample 2 and the ZnO NCs and NWs grown on the plasma-annealed sample 6 have the better crystalline quality. The peak positions and the full width at half maximum (FWHM) of the NBE are summarized in table 1. For the thermal-annealed samples, the NBE exciton peak position shifts to shorter wavelengths when increases the diameter of the ZnO NWs (i.e. when increasing the thickness of the Au-catalyst films), while for the plasma-annealed samples, the NBE exciton peak position shifts to longer
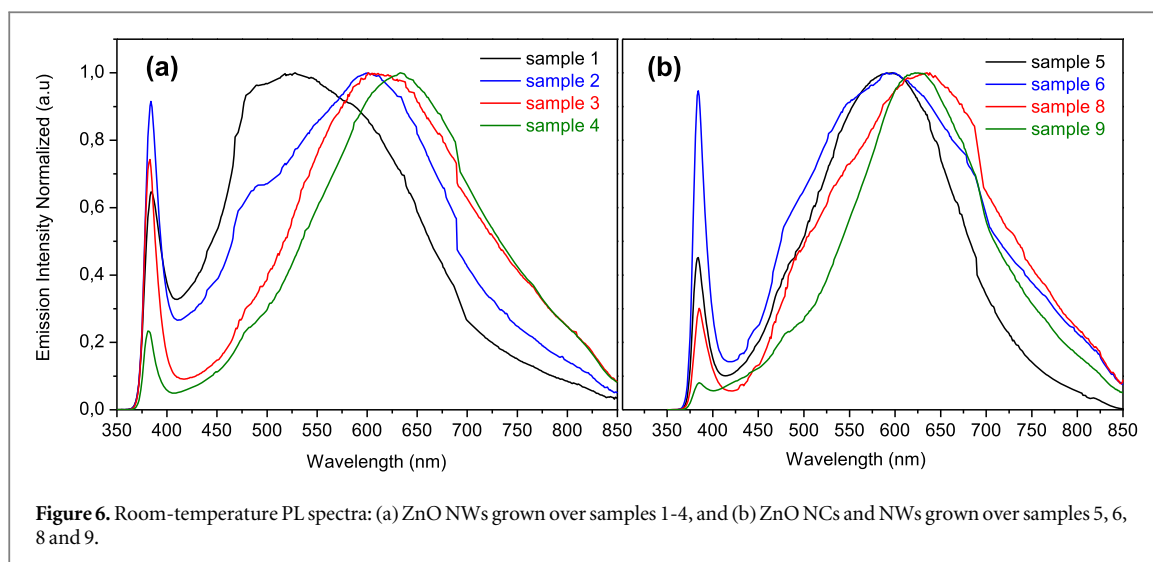
Figure 6. Room-temperature PL spectra: (a) ZnO NWs grown over samples 1-4, and (b) ZnO NCs and NWs grown over samples 5, 6, 8 and 9.

wavelengths when the thickness of the Au-catalyst films increases or the plasma power increases. One possible reason for the variations in the position of the NBE emission in the ZnO NCs and NWs is different concentrations of defects. Since the defect density on the surface is higher than in the bulk [28], spectral shifts due to different defect concentrations are expected to occur in nanostructures with different sizes and shapes due to different surface-to-volume ratios. The fact that the decay times in time-resolved PL measurements from ZnO NWs are size-dependent [29] is in agreement with the assumption of different defect levels/concentrations for nanostructures with different surface-to-volume ratios. Thus, the defects could affect the position of the maximum emission intensity of the NBE as well as the shape of the luminescence spectrum, which agrees with the different broadenings observed in the FWHM. Regarding to the broad emission band in the visible range, sample 1 has its maximum emission intensity peak position in the green region at around 520 nm (2.38 eV), while for samples 2, 3, 5 and 6 is shifted to the yellow region at around 590 (2.10 eV) and for samples 4, 8 and 9 to the red region at around 640 nm (2.00 eV). These broad emission bands in the visible region also exhibit a secondary peak, sometimes apparent as a shoulder, in the blue region at around 480 nm (2.58 eV). The variations shape and position in the visible region is also related to the kind of defects in the material [30]. We can assume that the shoulder observed in the blue region at around 480 nm is considered to be the result of the transition between Zn interstitials and Zn vacancies ($Zn_i \rightarrow V_{Zn}$) [31]; the green emission band at around 520 nm corresponds to the local level composed by oxide antisite defect O_{Zn} [32]; the yellow emission band at around 590 nm is a consequence of the radiative recombination processes associated with Au impurities introduced during the catalytic growth [12]; and the red emission band at around 640 nm is ascribed to the Zn interstitials [33]. For the thermal-annealed samples, the type of defects present in the sample show a redshift increasing the thickness of the Au-catalyst film, while for the plasma-annealed samples this redshift takes place increasing the plasma power from 50 to 100 W and does not depend on the thickness of the Au-catalyst. This could be associated with the chemical treatment by the plasma, at 50 W the NH_3 plasma promote the stabilization of uncoordinated Au atoms with NH_2 and NH allowing the introduction of Au impurities. In contrast at 100 W, the Au-catalyst is over damage promoting a competitive interchange of the CO with the NH_2, NH and NO_2 generating more Zn interstitials.

4. Conclusions

Au thin layers with different thicknesses were thermal or plasma annealed on AZO buffer layers over fused silica substrates in order to induce the catalyst-assisted growth of ZnO NCs and NWs. The thermal annealing generates a distribution of Au nanoclusters, and the plasma annealing induces a fragmentation of the Au thin film and an adsorption of NH_3, NH_2 and NH to the low coordinated Au atoms. The thickness of the Au films determines the diameter and density of the ZnO NCs and NWs obtained. For the thermal-annealed samples, thinner Au films promote the growth of high-density ZnO NWs with small diameter sizes while thicker Au films promote low-density ZnO NWs with larger diameters. Then, diffusion and coalescence of the Au nanoclusters on the AZO surface are the determining factors for the obtained ZnO NW density on the thermal-annealed samples. For the plasma-annealed samples the surface chemistry introduced by the presence of the NH_2 and NH competes with diffusion and coalescence of the Au nanoclusters on the AZO surface. Then, the NH_3 reduces the

oxygen availability because of the competition with other oxidation reactions, and as a consequence the conical shape is observed in the ZnO NCs obtained. The transmittance spectra of the ZnO NCs and NWs show a gradual increase from 375 to 900 nm due to the light scattering, which increases for shorter wavelengths approaching to the dimensions of the ZnO NCs and NWs. The PL emission spectra show the characteristic exciton peak in the UV at around 380 nm besides the defect-related band in the visible range with its maximum emission intensity peak positions at around 520, 590 and 640 nm.

Acknowledgments

References

[1] Das S K, Güell F, Gray C, Das P K, Grunwald R and McGlynn E 2014 ZnO nanorods for efficient third harmonic UV generation *Opt. Mater. Exp.* **4** 701–9

[2] Huang M H, Mao S, Feick H, Yan H Q, Wu Y Y, Kind H, Weber E, Russo R and Yang P D 2001 Room-temperature ultraviolet nanowire nanolasers *Science* **292** 1897–9

[3] Konenkamp R, Word R C and Schlegel C 2004 Vertical nanowire light-emitting diode *App. Phys. Lett.* **854** 6004–6

[4] Fan J, Hao Y, Munuera C, García-Hernández M, Güell F, Johansson E M J, Boschloo G, Hagfeldt A and Cabot A 2013 Influence of the annealing atmosphere on the performance of ZnO nanowire dye-sensitized solar cells *J. Phys. Chem.* C **117** 16349–56

[5] Zhou Y, Kelly P J, Postill A, Abu-Zeid O and Alnajjar A A 2004 The characteristics of aluminium-doped zinc oxide films prepared by pulsed magnetron sputtering from powder targets *Thin Sol. Films* **447–448** 33–7

[6] Liu Y, Zhao L and Lian J 2006 Al-doped ZnO films by pulsed laser deposition at room temperature *Vacuum* **81** 18–22

[7] El Manouni A, Manjón F J, Mollar M, Marí B, Gómez R, López M C and Ramos-Barrado J R 2006 Effect of aluminium doping on zinc oxide thin films grown by spray pyrolysis *Superlattices Microstruct.* **39** 185–90

[8] Lee S-H *et al* 2010 Al-doped ZnO thin film: a new transparent conducting layer for ZnO nanowire-based dye-sensitized solar cells *J. Phys. Chem.* C **114** 7185–92

[9] Zhang J and Que W 2010 Preparation and characterization of sol–gel Al-doped ZnO thin films and ZnO nanowire arrays grown on Al-doped ZnO seed layer by hydrothermal method *Sol. Energy Mater. Sol. Cells* **94** 2181–6

[10] Fan J, Güell F, Fàbrega C, Fairbrother A, Andreu T, López A M, Morante J R and Cabot A 2012 Visible photoluminescence components of solution-grown ZnO nanowires: influence of the surface depletion layer *J. Phys. Chem.* C **116** 19496–502

[11] Güell F, Martínez-Alanis P R, Khachadorian S, Zamani R R, Franke A, Hoffmann A, Wagner M R and Santana G 2016 Spatially controlled growth of highly crystalline ZnO nanowires by an inkjet-printing catalyst-free method *Mater. Res. Exp.* **3** 025010

[12] Güell F, Osso J O, Goni A R, Cornet A and Morante J R 2009 Direct imaging of the visible emission bands from individual ZnO nanowires by near-field optical spectroscopy *Nanotechnology* **20** 315701

[13] Méndez-Reyes J M, Monroy B M, Bizarro M, Güell F, Martínez A and Ramos E 2015 Gold as intruder in ZnO nanowires *Phys. Chem. Chem. Phys.* **17** 21525–32

[14] Roso S, Güell F, Martínez-Alanis P R, Urakawa A and Llobet E 2016 Synthesis of ZnO nanowires and impacts of their orientation and defects on gas sensing properties *Sensors Actuators* B **230** 109–14

[15] Govatsi K, Chrissanthopoulos A, Dracopoulos V and Yannopoulos S N 2014 The influence of Au film thickness and annealing conditions on the VLS-assisted growth of ZnO nanostructures *Nanotechnology* **25** 215601

[16] Reparaz J S, Güell F, Wagner M R, Callsen G, Kirste R, Claramunt S, Morante J R and Hoffmann A 2010 Recombination dynamics in ZnO nanowires: surfaces states versus mode quality factor *Appl. Phys. Lett.* **97** 133116

[17] Fandiño J, Crespo A, Santana G, Rodríguez-Fernández L, Alonso J C, García-Sánchez M F, Ortiz A, Vigil O, Lopez-Suarez A and Oliver A 2009 Plasma-induced size reduction in Au nanoclusters embedded in a dielectric matrix *Sci. Adv. Mater.* **1** 249–51

[18] Fandiño J, García-Sánchez M F, Santana G, Crespo A, Alonso J C and Oliver A 2008 Correlations between microstructure of plasma-modified gold nanoclusters and their optical properties *Superlattices Microstruct.* **43** 454–7

[19] Hussain A, Curulla-Ferré D, Gracia J, Nieuwenhuys B E and Niemantsverdriet J W 2009 DFT study of CO and NO adsorption on low index and stepped surfaces of gold *Surf. Sci.* **603** 2734–9

[20] Liu R, Shen W, Zhang J and Li M 2008 Adsorption and dissociation of ammonia on Au (111) surface: a density functional theory study *App. Surf. Sci.* **254** 5706–9

[21] Il'chenko N L 1976 Catalytic oxidation of ammonia *Russ. Chem. Rev.* **45** 1119–35

[22] Brewster M M, Zhou X, Lim S K and Gradečak S 2011 Role of Au in the growth and nanoscale optical properties of ZnO nanowires *J. Phys. Chem. Lett.* **2** 586–9

[23] Fajín J L C, Cordeiro M N D S and Gomes J R B 2010 DFT study on the reaction of NO oxidation on a stepped gold surface *Appl. Cat.* A **379** 111–5

[24] Liu X-J and Hamilton I 2014 Adsorption of small molecules on helical gold nanorods: a relativistic density functional study *J. Comp. Chem.* **35** 1967–71

[25] Johnson P B and Christy R W 1972 Optical constants of the noble metals *Phys. Rev.* B **6** 4370–9

[26] Gupta R, Dyer M J and Weimer W A 2002 Preparation and characterization of surface plasmon resonance tunable Au and silver films *J. Appl. Phys.* **92** 5264–8

[27] Yousefia R and Zak A K 2011 Growth and characterization of ZnO nanowires grown on the Si(1 1 1) and Si(1 0 0) substrates: optical properties and biaxial stress of nanowires *Mater. Sci. Semicond. Process.* **14** 170–4

[28] Göpel W and Lampe U 1980 Influence of defects on the electronic structure of zinc oxide surfaces *Phys. Rev.* B **22** 6447–52

[29] Reparaz J S, Güell F, Wagner M R, Hoffmann A, Cornet A and Morante J R 2010 Size-dependent recombination dynamics in ZnO nanowires *Appl. Phys. Lett.* **96** 053105

[30] Güell F, Martínez-Alanis P R, Khachadorian S, Rubio-Garcia J, Franke A, Hoffmann A and Santana G 2016 Raman and photoluminescence properties of ZnO nanowires grown by a catalyst-free vapor-transport process using ZnO nanoparticle seeds *Phys. Status Solidi* B **253** 883–8

[31] Lin B, Fu Z and Jia Y 2001 Green luminescent center in undoped zinc oxide films deposited on silicon substrates *Appl. Phys. Lett.* **79** 943–7

[32] Srivastava A K and Kumar J 2013 Effect of zinc addition and vacuum annealing time on the properties of spin-coated low-cost transparent conducting 1 at% Ga–ZnO thin films *Sci. Technol. Adv. Mater.* **14** 065002

[33] Gomi M, Oohira N, Ozaki K and Koyano M 2003 Photoluminescent and structural properties of precipitated ZnO fine particles *Japan. J. Appl. Phys.* **42** 481–5